Influence of thermal treatment on the structure and electrical conductivity of thermally expanded graphite

Alina Madalina Darabut[a], Yevheniia Lobko*[a], Yurii Yakovlev[a], Miquel Gamón Rodríguez[a], Kateřina Veltruská[a], Břetislav Šmíd[a], Peter Kúš[a], Jaroslava Nováková[a], Milan Dopita[d], Maryna Vorokhta[b], Vladimír Kopecký Jr.[c], Marek Procházka[c], Iva Matolínová[a], Vladimír Matolín[a]

[a]Charles University, Faculty of Mathematics and Physics, Department of Surface and Plasma Science, V Holešovičkách 2, 180 00 Prague 8, Czech Republic
[b]Czech Academy of Sciences, Institute of Rock Structure and Mechanics, Department of Geochemistry, V Holešovičkách 94/41, 182 09 Prague 8, Czech Republic
[c]Charles University, Faculty of Mathematics and Physics, Institute of Physics, Ke Karlovu 5, 121 16 Prague 2, Czech Republic
[d]Charles University, Faculty of Mathematics and Physics, Department of Condensed Matter Physics, Ke Karlovu 5, 121 16 Prague 2, Czech Republic

*Corresponding author at: Department of Surface and Plasma Science, Faculty of Mathematics and Physics, Charles University, V Holešovičkách 2, Prague, 18000, Czech Republic

Yevheniia Lobko
Tel: +(420) (95155-2251)
e-mail: yevheniia.lobko@mff.cuni.cz (Y. Lobko)

Suggestive reviewers

Professor Chung, Deborah D.L.

State University of New York (SUNY) System, Department Mechanical & Aerospace Engineering, Buffalo, NY, USA
e-mail: ddlchung@buffalo.edu
Prof. Chung, Deborah D.L. is a specialist in materials and their characterization. She has authored or co-authored over 550 archival international peer-reviewed journal papers, in addition to 8 books, which include "Carbon Composites" (2nd Ed., Elsevier, 2016), "Functional Materials" (World Sci., 2010) and "Composite Materials" (2nd Ed., Springer, 2010).

Professor Inagaki, Michio

Hokkaido University, 228-7399 Nakagawa, Hosoe-cho, Kita-ku, Hamamatsu 431-1304, Japan
e-mail: im-ii@ace.ocn.ne.jp
Prof. Inagaki, Michio is an expert in carbon materials with more than 160 publications about the carbon-based materials, as well as several books.

Dr. Motlagh, Ghodratollah Hashemi

College of Engineering of University of Tehran, Advanced Polymer Materials & Processing Lab, School of Chemical Engineering, Tehran, Iran
e-mail: ghmotlagh@ut.ac.ir
Dr. Motlagh, Ghodratollah Hashemi is an expert in graphite intercalated compounds and expanded graphite.

Abstract

Thermally expanded graphite (TEG) is a promising filler beneficial to electrically conductive materials due to its high electrical conductivity, low density, and cost. In this work, the electrically conductive TEG was prepared by thermal treatment of the expandable graphite in the range of temperatures from 400 to 800 ºC in air. Effects of the temperature treatment on the morphology and chemical structure of TEG were thoroughly characterized. Thermal treatment of the expandable graphite resulted in thermally expanded graphite formation with up to 6 times higher electrical conductivity than the precursor. Optimal conditions of thermal treatment were established at 600 ºC providing material with the highest electrical conductivity, high expansion volume, and a well-ordered and defect-less structure.

Keywords: Thermally expanded graphite; Thermal treatment; Ordered and porous structure; electrical conductivity.

1. Introduction

Nowadays, a tremendous pace of scientific progress requires advanced polyfunctional materials, which can be extensively used in various fields of science and technology. Among such materials, including carbon nanotubes, nanocoins, nanofibers, or graphene, a thermally expanded graphite (TEG) is one of the most promising due to its outstanding electrical and thermal conductivity, low density, high surface area, low price, etc. These properties provide TEG with virtually endless applications in supercapacitors [1], thermally conductive materials for energy storage [2–5], adsorbents [6–8], lithium-ion batteries [9], catalyst supports [9], fuel cells [10–14], polymer composites [12–20], etc. [9].

As a precursor for TEG, the expandable graphite (EG) intercalated with an inorganic acid is used [8,21,22]. Upon rapid acid evaporation by heat [23–27] or microwave treatment [28,29], the interlayer spacing in EG drastically increases, forming a worm-like TEG structure with low density and high surface area [9]. Therefore, the procedure and conditions of TEG preparation affect the expansion, structure, and properties of the resulting materials [16,30–32]. In particular, the temperature of thermal treatment [23,33–35] and reducing/oxidizing properties of the atmosphere [36] have a strong influence, paving the way for optimization and/or alteration of TEG properties.

The temperature of EG treatment influences such structural characteristics of TEG as graphite expansion volume [23], density, and porosity [35,37,38]. Thus, usually, the expanded volume significantly increases with temperature rising [23] and goes through the maximum at different temperatures (80 ºC [34], 500 ºC [7], or 1000 ºC [23]). The density is another parameter affected by the temperature, which changes with increasing the temperature [38]. At the same time, the surface area of expanded graphite increases with temperature racing up to 600 ºC and then decreases [25,38]. The growth of the pore volume and diameter of the graphite particles with the rising of the treatment temperature from 700 to 900 ºC was also detected [37]. The growth of the above-mentioned surface parameters is usually connected to the increasing distance between the layers (d-spacing) in graphite after thermal treatment [23,39,40]. On the other hand, changes in chemical structure and the number of defects of TEG stem from the temperature and reducing/oxidizing atmosphere of the treatment [36,41]. Thus, the thermal treatment causes both oxidation or de-oxidation of the expanded graphite with a formation of graphene oxide [42], removal of amorphous phase and decrease of the number of defects upon annealing [34,43], formation of oxygen-containing functional groups, and corresponding change of C/O ratio [44,45]. However, as was shown in [37] by using Fourier-transform (FTIR) spectroscopy, the different temperature does not affect the formation of functional groups.

Alteration of structural and chemical characteristics of TEG may result in different macroscopic properties of the material. Thus, expanded volume and porosity of TEG affect the sorption capacity [7,8,23,37], and electrochemical properties [46]. Electrical conductivity may be affected by the presence of sp^3 hybridized carbon, oxygen-containing groups, and/or defects. Moreover, increasing the graphite expansion volume could tangibly reduce the electrical conductivity of the graphite, due to the increase of the porosity and contact resistance between layers [9,34].
Despite numerous studies on TEG morphology and chemical structure, the investigation of TEG properties is incomplete and unsystematic. Especially, the investigation of the electrical properties of TEG is scarce and relates mostly to the conductivity of the polymer composites filled with TEG [47–51] or other materials based on TEG [52,53]. Therefore, in the current work, we will focus on the effect of the treatment at different temperatures on the TEG thermal expansion, morphological and chemical structure, and their influence on the electrical conductivity of the obtained materials. Moreover, the thermal expansion will be conducted in the air to demonstrate the applicability of such an atmosphere for the high-scale and low-cost production of TEG.

2. Material and methods

2.1. Preparation of thermally expanded graphite

Expandable graphite (EG) flakes (ES 350 F5), impregnated with sulfuric acid, (Graphit Kropfmühl GmbH Company, Germany) were used as a precursor for obtaining the thermally expanded graphite. The average size of flakes is around 300 μm, and carbon content is 98 %, according to the supplier information. TEG were prepared by a thermal treatment in an oxidation atmosphere from the EG flakes. The EG flakes were heated up in a porcelain crucible in a muffle furnace (MLW, Germany). The temperature varied from 400 to 800 ºC and the gradual rate of temperature change was 30 ºC min^{-1}. The sample was held at the chosen temperature for 1 minute and cooled down. Hereinafter, the TEG, which were obtained, e.g., at 400, 500, 600, 700, and 800 ºC, would be marked as TEG400, TEG500, TEG600, TEG700, and TEG800, respectively. The heating range was chosen according to the thermal gravimetrical analysis (TA Instruments, USA) of EG. The expansion process was started at a temperature higher than 400 ºC (Fig. S1), which corresponds to the value of the TEG expanded volume (Fig. S2a). It is worth noting that the heating in the air at temperatures higher than 800 ºC was not reasonable due to the critical decrease of the sample mass because of EG degradation in an oxidizing atmosphere. The weight losses of the TEG are equal to 29 ± 3 %, 27 ± 1 %, and 92 ± 8 %, for TEG500, TEG600, and TEG 800, respectively. Such effect can also be observed in the SEM images (Fig. S4d, e).

2.2. Physical and chemical characterization

The expanded volume, bulk density, and wettability (via contact water angle) of the samples were measured and calculated (see the SI, Fig. S2, S3, and S5).
A JEOL 2200 FX transmission electron microscope with 200 kV acceleration voltage applied was used to observe the structure of graphite nanolayers (GNL) sheets of prepared TEG. For transmission electron microscopy (TEM) measurements, samples of GNL were prepared from TEG by sonication of TEG dissolved in ethanol (96%, Penta, Chem. Unlim.) in the pulse mode on-off time 3s at 20 kHz (Bandeling Sonopuls HD 3100, Germany) for 20 min. The crystalline structure of the GNL was analyzed using Digital Micrograph software [54].
The morphology and size of EG flakes and TEG particles were analyzed using a field emission scanning electron microscope (FE-SEM, Mira III, TESCAN ORSAY HOLDING, Czech Republic), operating at 30 keV beam energy. The chemical composition of the samples (in pellet form) was determined by energy-dispersive X-ray spectroscopy (EDX) using a Quantax EDX detector (Brucker,

Germany) at the 5 keV electron beam. Here and after the formation of the pellets, the powders were pressed onto cylindrical pellets (diameter 1.6 cm and 0.1–0.2 mm thickness) by a mechanical press (H-62, Trystom, Czech Republic) with a force of 80 kN.

Raman measurements were performed using an HR800 Raman micro-spectrometer (Horiba Jobin Yvon, France) with a 633 nm He-Ne excitation laser (20 mW) focused with a 50× microscope objective with a long working distance (N.A. 0.55, Olympus, Japan). Spectra were integrated for 120 s and collected using a 300 grooves mm^{-1} grating and liquid nitrogen cooled CCD detector with resolution ~8 cm^{-1} (the wavenumber scale was calibrated using a Si sample). Ten spectra on each of the samples (EG flake, TEG500, TEG600, and TEG800) were measured at different places on the powder samples. The averaged spectra of the samples were normalized using the integrated absolute area of the 2D peak. Additionally, the intensity of the peaks was obtained using the same mathematic analysis (integration of the absolute area). The in-plane crystallite size (L_a) was calculated using the modified Tuinstra and Koenig equation (Eq. S6) [55,56].

X-ray diffraction (XRD) measurements were performed using an Empyrean 2 diffractometer (Panalytical, Netherlands) equipped with a Cu X-ray tube (λ = 1.5406 Å). To reduce the influence of the preferential orientation of crystallites, the powder was inserted into glass capillaries and measured in transmission mode. The measured XRD patterns were fitted using the whole powder pattern fitting procedure (Rietveld method) by the combination of graphitic and turbostratic carbon phases, to obtain the information about the lattice parameters and size of coherently diffracting domains.

Infrared spectra of the samples were recorded with a Vector 33 FTIR spectrometer (Bruker, Germany) using a standard MIR source, a KBr beam-splitter, and a DTGS detector. 400 scans were collected with 4 cm^{-1} spectral resolution and the Blackman-Harris 3-term apodization function. The spectrometer was purged by dry air during all experiments. 7 mm KBr-pellets of TEG powder were prepared using KBr for infrared spectroscopy (Specac, United Kingdom) mixed with a small amount of the graphite samples (1:100). The spectra were normalized on the ν(C–H) bond at 2800–3000 cm^{-1}.

The surface chemical compositions of the EG and TEG were measured by an X-ray photoelectron spectroscopy (XPS) (Specs, Germany) using a laboratory XPS spectrometer equipped with a hemispherical analyzer Phoibos 150 (Specs, Germany) and Mg Kα X-ray source in ultrahigh vacuum (UHV) conditions. The pellets were stuck to the stainless-steel sample holder using copper tape. During XPS measurements, the core-level spectra of C *1s*, O *1s*, S *2p,* N *1s,* and Na *1s* were recorded with a pass energy of 20 eV, step size of 0.05 eV, and dwell time of 200 ms. The XPS spectra were processed with KolXPD software [57]. The XPS peaks were processed using Voigt waveforms for C *1s* and O *1s* core-level spectra, and Double Voigt waveform for S *2p*. Moreover, for the asymmetry of the sp^2 carbon bond peak [58], the Doniach- Šunjić lineshape combined with the Gaussian function was used. All spectra were fitted after subtraction of the Shirley background. The peaks were normalized to the area of the full-wave of each element. The silicone oxide peak was subtracted from the O *1s* core-level peaks.

The specific surface area and porous structure of the EG and TEG were analyzed using the nitrogen adsorption isotherms (Thermo Scientific™ Surfer, USA). Samples outgassing was performed at 75 ºC overnight under a vacuum using a turbopump, then the blank measurement was done with helium, and the adsorption with nitrogen at –196 ºC. The N_2 adsorption isotherms measured were fitted with the Brunauer-Emmett-Teller (BET) equation to determine the specific surface area (S_{BET}) ($m^2\,g^{-1}$). The mesopore volume (V_{meso}) was calculated (Eq. S6). The maximum diameter of mesopores ($D_{meso(max)}$) was estimated by applying the Barrett-Joyner-Halenda (BJH) method to the N_2 adsorption isotherm.

The electrical resistivity (ρ) of the EG and TEG samples, in pellet form, was measured by impedance spectroscopy via the four-point collinear probe arrangement using an SP-150-1 potentiostat (BioLogic Science Instruments, France). The electrical conductivity at direct current (σ) was

calculated taking into account the measured resistivity, and the correction factors based on the ratio of the sample diameter and the distance between the gold probes (s) and the ratio of sample thickness to probe spacing, according to the Smits and Uhlir equations [59–61]. The scheme of the four-point probe measurements (Fig. S7) and the used equations (Eq. S2-4) are presented in SI.

3. Results and discussions

3.1. Influence of the temperature on TEG formation

3.1.1. Scanning electron microscopy

Fig. 1 presents the morphology of EG and obtained TEG according to SEM. Fig. 1a demonstrates EG compact flakes, formed from several layers. The interlayer structure of EG expands along the c-axis, under temperature, and TEG, widely known as a worm-shaped form, (Fig. 1b, Fig. S4) are obtained. It is worth drawing attention to the appearance of defects for TEG700 and TEG800 (Figs. S4d, e). Such effect is probably caused by the partial thermally oxidative degradation (Fig. S1) [62–64], which corresponds to the decreasing of expanded volume (Fig. S2a).

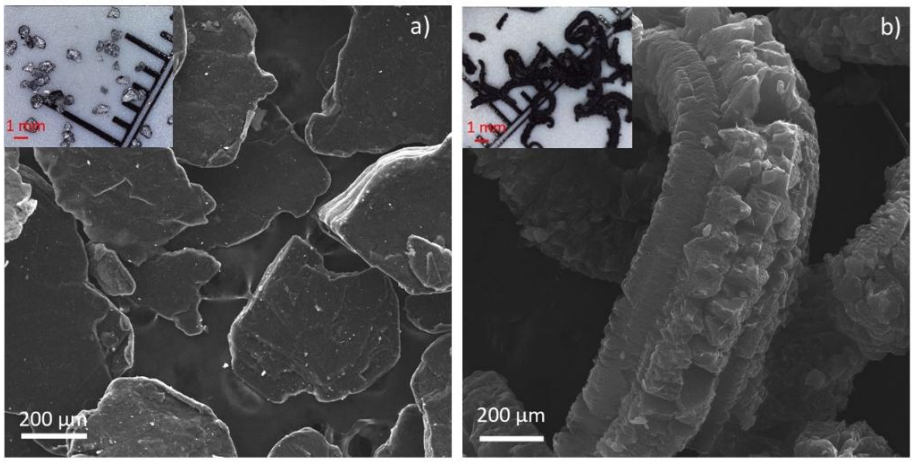

Fig. 1. FE-SEM images of EG flakes (a) and TEG600 (b). Inserts represent optical microscope images.

3.1.2. Transmission electron microscopy

Fig. 2 shows an example of the structure and heterogenous crystallinity of graphene nanolayers (GNL), which form the TEG. TEG obtained at different temperatures have a similar amorphous-crystalline structure. As one can see, the interlayer spacing of GNL is equal to around 0.21 nm.

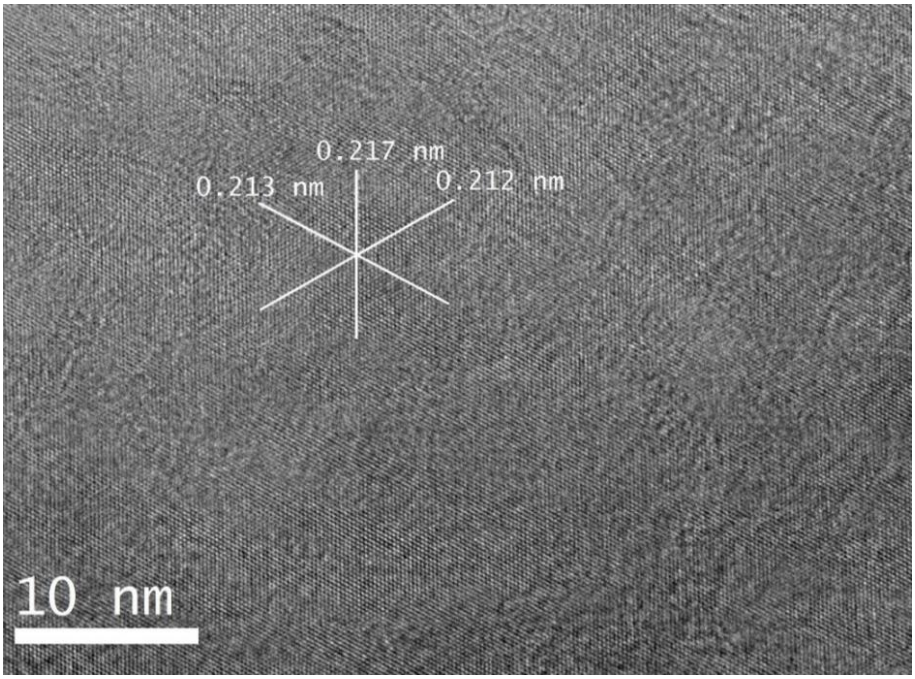

Fig. 2. TEM image of TEG600.

Fig. S6b displays the Fast Fourier Transform (FFT) diffraction pattern of the TEG image acquired on TEG600 with six very well defined inner spots [(100), (1–10), (0–10), (–100), (–110), (010)] and other outer less intense spots, corroborating the existence of a single layer of GNL. According to the FFT diffraction pattern, the measured interplanar distances are equal to 0.216 nm, 0.124 nm and, 0.108 nm (Fig. S6a inserted figures), which corresponds to the diffraction pattern of graphite with the hexagonal cell, space group P 6_3/mmc, and [0.0.1] zone axis (Fig. S6c), obtained from database [65]. Moreover, the calculated d-spacing for hexagonal graphite structure with Bravais lattice with the lattice parameters a (0.246 nm) and c (0.671 nm) [66] are equal to 0.213 nm, 0.123 nm, and 0.107 nm [67], which are similar to the TEG600 parameters above.

3.1.3. Raman spectroscopy

To gain more insights into the structure of TEG, Raman spectroscopy was used. Fig. 3 shows the Raman spectra of EG flakes and obtained TEG. The features at 1330, 1576, and 2682 cm^{-1} correspond to the D, G, and 2D bands, respectively, which are the most characteristic bands of a graphitic material [68]. EG flakes have two additional peaks, D' and D+D' at 1608 cm^{-1} and 2914 cm^{-1}, respectively. The fitting of the 2D bands (Fig. S8), gives two deconvolution peaks, $2D_1$ and $2D_2$ at 2683 and 2644 cm^{-1}, respectively [69]. It must be pointed that *Cançado et al.* [70] have presented the two-peak shape of this band in bulk graphite as a result of the convolution of an infinite number of peaks. More detailed information about the bands can be found in SI.

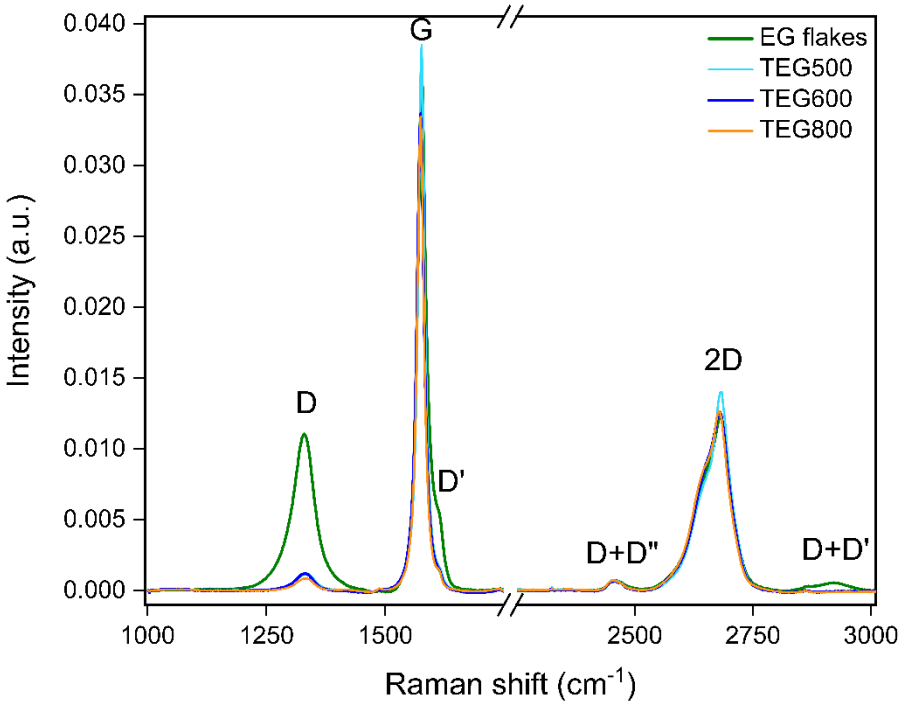

Fig. 3. Raman spectra of EG flakes, TEG500, TEG600, and TEG800.

The effect of thermal treatment appears in the decreasing of D peak and vanishing of the D' shoulder in TEG samples compared with EG flakes (Fig. 3). This effect points out that the part of the TEG crystalline phase increases [71]. However, a higher intensity ratio of the D and G bands (I_D/I_G) of EG (0.7), compared with such of TEG (0.08, 0.08, 0.06 for TEG500, TEG600, and TEG800, respectively) indicates a higher quantity of defects on EG structure (Table S1) [69,72]. A possible explanation of the existence of these defects in the EG flakes might be the presence of intercalated compounds (SO_4^{2-}) which are evaporated at high temperatures, forming the more ordered structure of TEG. Additionally, the calculated crystallite size (L_a) [55] (Table S1) also drastically increases after thermal treatment (from 55 to 467 nm) and it is largest at 800 ºC (615 nm).

3.1.4. X-ray diffraction

The structure of the EG and TEG samples was analyzed by the XRD technique. The XRD patterns of studied materials (Fig. *4*) contain peaks from crystalline, graphitic, and diffuse, asymmetric profiles from turbostratic carbon structures [73]. The peaks of graphitic phase show significant broadening anisotropy (broad 00l and narrow hk0 peaks) representing the small size of coherently diffracting domains in 00l direction and big crystallite size in the plane of graphitic sheets hk0. Moreover, the graphitic phase (002) peak of EG sample at 26.4º has a wide asymmetrical shape [73]. After the thermal treatment, the maxima of 002 peaks slightly shifted to 26.5º, similar tendency is seen in [74], the peaks' intensity increased, and the crystallite sizes increased from 12.1 nm up to 54.9 nm (see Table S1). The same tendency is observed to (004) and (006) reflections. This reveals that EG was expanded, and, at the same time, the layered graphite's structure is preserved, but became more homogeneous and ordered with the d-spacing between the graphene layers of around 0.3363 nm [15,75]. The peaks shifting could be pointed on the slight decreasing of the d-spacing due to the SO_2 evaporation after the thermal treatment, which is substantiated by other data. The temperature of the treatments does not drastically influence the structure of the materials. The refined lattice parameters *a* and *c* of the graphitic phase (Fig. S9) correspond well with the tabulated values of graphite lattice

parameters [66] and correlate with the ones chosen for the d-spacing calculated from the TEM image (Fig. S6).

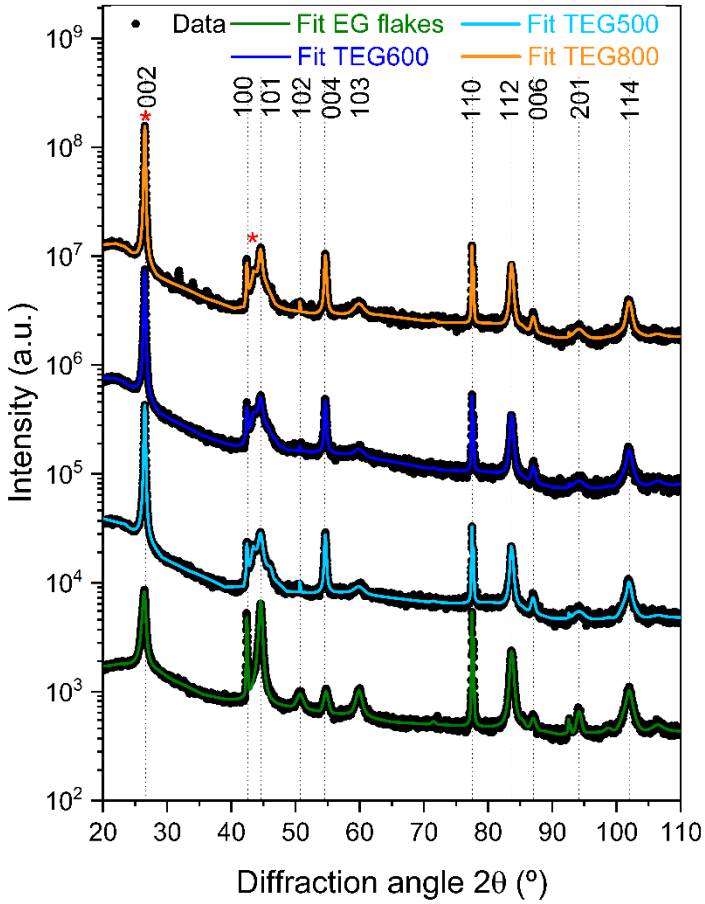

Fig. 4. Measured (black circles) and fitted (lines) XRD patterns of EG flakes, TEG500, TEG600, and TEG800 samples. The diffraction peak positions of graphitic phase, together with their Miller indices are depicted in the figure. The positions of turbostratic carbon (002) and (10) peaks are marked with asterisk.

Furthermore, the existence of turbostratic structure is demonstrated by the presence of (002) and (10) peaks in Fig. 4 [76,77]. A closer look at the diffraction patterns shows an intensity increase of the broad, amorphous peak between 20-35º. Therefore, it indicates an increment in the fraction of disorganized/amorphous carbon during the thermal treatment.

3.1.5. Nitrogen adsorption analysis

Table 1 shows some parameters, obtained from the nitrogen adsorption analysis. After the thermal treatment, BET specific surface area (S_{BET}) drastically increases from 0.05 up to 33 $m^2 g^{-1}$. For comparison, data available in the literature show that the surface area of TEG obtained at 700–900 ºC, 900 ºC, and 1000 ºC, reaches 25–31, 45, and 40 $m^2 g^{-1}$, respectively [37,78,79].

Table 1. Surface parameters according to the nitrogen adsorption analysis.

Sample	S_{BET} ($m^2 g^{-1}$)	$D_{meso(max)}$ (nm)	Monolayer volume ($cm^3 g^{-1}$)	V_{micro} ($cm^3 g^{-1}$)	V_{meso} ($cm^3 g^{-1}$)
EG flakes	0.05	—	—	—	0.0045

TEG500	22	2.6	5	0.0078	0.0876
TEG600	25	2.7	5.7	0.0078	0.1262
TEG800	33	3.3	7.6	0.0112	0.1870

Fig. S10 exposes the mesopores distribution calculated by the BJH method from the adsorption branch of TEG500, TEG600, and TEG800. It is observed that TEG500 and TEG600 have very similar pore size distribution, with a maximum diameter of mesopores 2.6 and 2.7 nm, respectively, but slightly different mesopores volumes. A possible explanation for these results might be that the temperature range of 500–600 ºC does not significantly affect the TEG samples, as is observed in all nitrogen adsorption parameters. For TEG800, the maximum diameter of mesopores is calculated to be 3.3 nm. Similar behavior was observed in [37], where the mesopore size diameter is smaller at a lower temperature of the thermal treatment. Furthermore, the results of this analysis show that the temperature process directly affects both the surface area and the formation of the pores.

3.2. Chemical structure analysis

3.2.1. Fourier-transform infrared spectroscopy

The chemical structure of the samples was analyzed using FTIR spectroscopy. Fig. 5 demonstrates FTIR spectra of EG flakes and the TEG prepared at different temperatures.

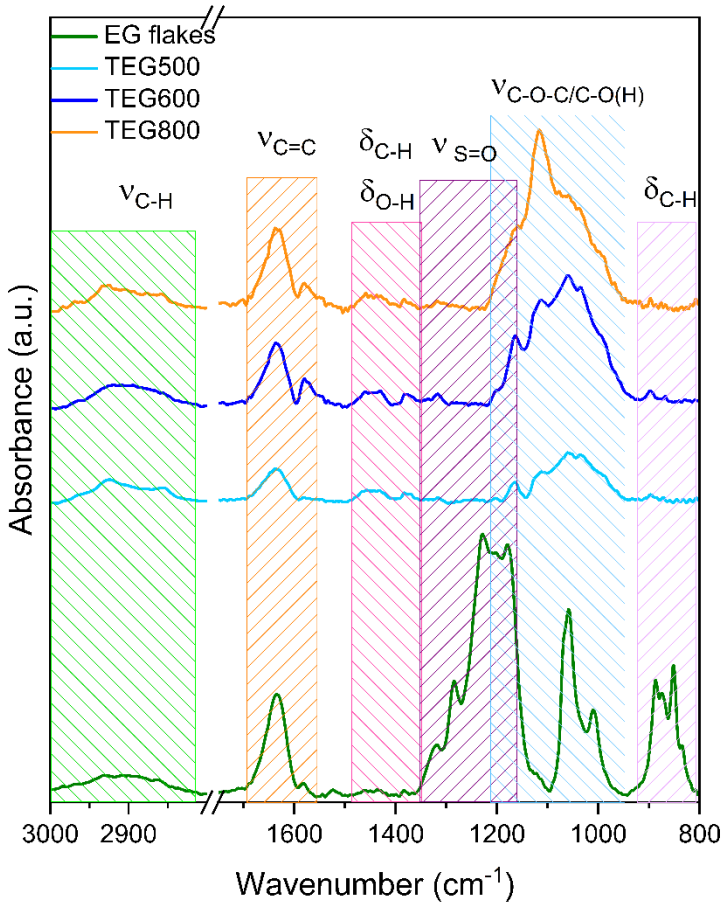

Fig. 5. FTIR spectra of EG flakes, TEG500, TEG600, and TEG800.

All samples have bands at 2923 cm^{-1}, and 2855 cm^{-1}, which are ascribed to C–H sp^3 asymmetric and symmetric stretching, respectively [80]. The peaks at 1635 and 1580 cm^{-1} are assigned to the C=C alkene and aromatic stretching, respectively [80–82]. It is widely known that the graphitic materials

have two strong absorption bands around 1580 cm^{-1} and 1360 cm^{-1}; moreover, these bands coincide with the bands observed in Raman spectra [82,83]. At low frequencies, in the range of 900–800 cm^{-1}, the out-of-plane vibrations of C–H species are detected [84–86].

Furthermore, EG flakes have the asymmetric and symmetric stretching vibration of sulfate bonds at 1287 and 1190 cm^{-1}, respectively [81,82,87]. Above mentioned vibrations are invisible at the spectra of TEG because of the vaporization of SO_2 at high temperatures during the thermal treatment [88]. Instead, for TEG samples the ether (C–O–C) and alcohol (C–O(H)) stretching vibrations appear in the range 1200–1000 cm^{-1} [82].

3.2.2. X-ray photoelectron spectroscopy and energy dispersive X-ray spectroscopy

The chemical surface composition of EG flakes and TEG was characterized by XPS. Fig. S11 shows the XPS survey spectra of the samples marking the peaks of C *1s*, O *1s*, S *2p*, N *1s,* and Na *1s*.

Table 2 shows the atomic composition of the samples. It is seen (Fig. S11, Table 2), that for all TEG samples the amount of C increases (up to 1.3×) while the amount of O and S drastically decreases (to 9 and 16×), compared with EG. The O and S contents decrease due to its evaporation as SO_2 during the thermal exfoliation [89]. Moreover, the increasing of the treatment temperature from 500 to 800 ºC enhances these effects for both surface (XPS) and bulk (EDX) composition of the samples (Table 2). The samples contain the traces of sulfur (Fig. S12), sodium, and nitrogen owing to the chemical process of obtaining EG flakes. Fig. 6 and Fig. S13 demonstrate the XPS fitting of the C *1s*, O *1s*, and S *2p* core-level spectra of EG flakes and TEG, obtained at the different temperatures.

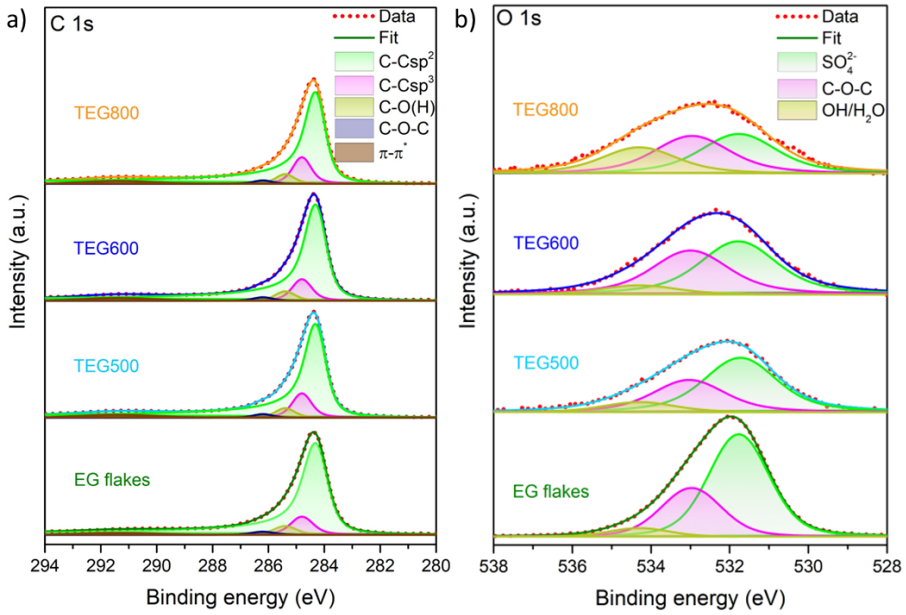

Fig. 6. Measured (red circles), fitted states (filled lines), and the sum of the fits (lines) of XPS peaks of the core levels: C *1s* (a), and O *1s* (b).

Table 2. The atomic composition of the samples. Concentrations obtained from XPS are written first, followed by values from EDX written in the bracket.

XPS (EDX)				
Sample	C at%	O at%	S at%	C/O
EG	74.6 (94.6)	22.3 (4.8)	3.1 (0.6)	3.4 (19.7)
TEG500	97.4 (97.2)	2.5 (2.2)	0.2 (0.3)	39.0 (44.2)
TEG600	96.6 (98.3)	3.2 (1.3)	0.2 (0.2)	30.5 (75.6)
TEG800	96.5 (99.1)	3.2 (0.8)	0.2 (0.05)	29.7 (123.9)

The states observed at binding energies of 284.3, 284.8, 285.4, 286.2, and 291.4 eV assigned to the presence of bonds C–C sp^2, C–C sp^3 [58], C–O(H), C–O–C [90–92], and π-π* transitions [42], respectively. Fig. 6b demonstrated O *1s* deconvolution peaks of EG flakes with three states at 531.8, 533.0, and 534.3 eV. These peaks correspond to SO_4^{2-} species [93], C–O(H) bonded to both aliphatic and aromatic carbon [21,43,44,94], and the so-called "intercalated adsorbed water molecules", trapped inside the graphite layers as a consequence of samples exposure to air after the thermal treatment [21,44,95,96], respectively.

The total C/O ratio after thermal treatment grows from 3.4 to 39.0 (from EG flakes to TEG500, respectively) (Table 2). With the temperature rising the C/O ratio decreases to 29.7, caused by partial surface oxidation of the TEG at a higher temperature. For comparison, one can find in the literature that XPS data on similar systems show the C/O ratio of 9.4 at 500 ºC [42], 6.8 at 600 ºC [45], 24 at 1000 ºC in the inert atmosphere [43], and 34.7 at 1050 ºC [97]. And, consequently, the obtained C/O ratio is higher at a lower temperature and in air. Moreover, the C–C/C–O ratio is stable (10.3–10.8) (Table S2). It is the substantial effect, that this variant of thermal treatment does not significantly change the amount of above-mentioned groups in all samples. This parameter means that the materials will have fewer defects and, as a result, should have a higher electrical conductivity value, at the more cost-efficient way of the sample preparation (comparable low temperature, without reducing atmosphere).

3.3. Electrical conductivity analysis

Fig. 7 shows the electrical conductivity of the EG flakes and TEG, obtained at different temperatures.

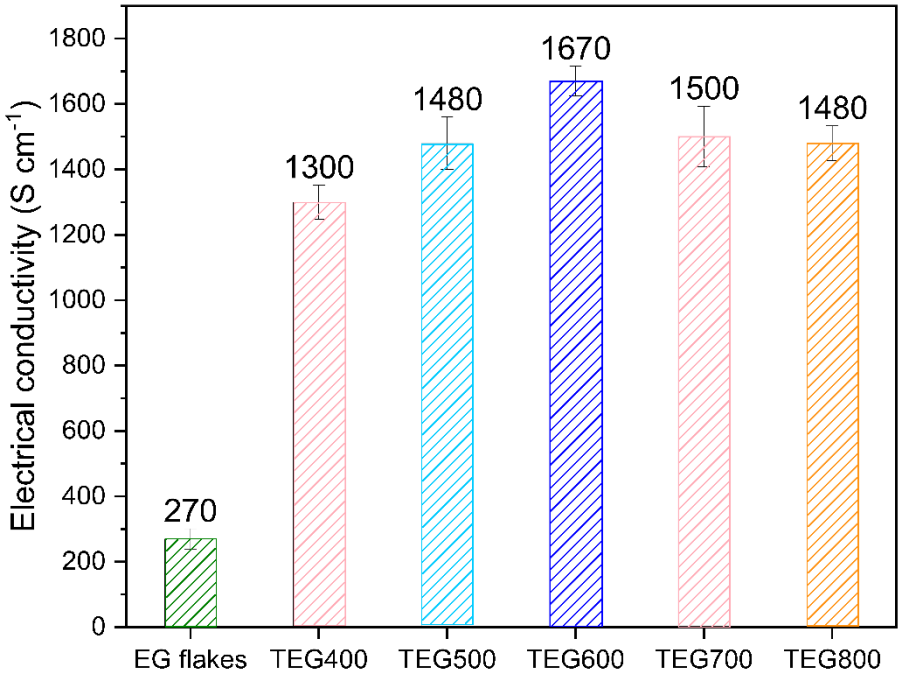

Fig. 7. Electrical conductivity of the EG flakes and TEG obtained at different temperatures.

It is detected that the values of the TEG electrical conductivity are more than five times higher than EG flakes' one. For comparison, the measured values of the electrical conductivity for the natural and synthetic graphite are equal to 320 and 700 S/cm, respectively. With the temperature rising the values of electrical conductivity grow up and reach their maximum at 600 ºC treatment, i.e., for TEG600. After 600 ºC the values of the electrical conductivity of the materials start to decrease. Such behavior entirely corresponds to the expansion volume pattern (Fig. S2a), i.e., thermal expansion of

the EG increases the number of the electrically conductive channels. On the opposite, the appearance of defects at temperatures higher than 700 ºC according to SEM images (Fig. S4d, e) decreases the number of such channels and leads to lower electrical conductivity levels. It is accompanied by changing crystalline size according to the Raman and XRD analysis (Table S1), and the preservation of carbonaceous structure after thermal treatment (Table S2).

4. Conclusions

The systematic study on properties of TEG prepared by thermal treatment of EG presented in this work points to the fact that the temperature of thermal treatment (in the range of 400–800 ºC) affects the morphology and chemical structure of TEG, and, consequently, the electrical conductivity of the materials. The detailed analysis of the thermal treatment influence on the structure of the materials showed that prepared TEG had a more ordered structure with a lesser number of defects, higher crystalline phase and size of the crystallite, higher surface area and porosity, higher surface and bulk carbonization rate, etc. The increase of the treatment temperature leads to the slight growth of the surface area and the mesopore sizes of TEG, and a reduction of the surface C/O ratio. At temperatures higher than 700 ºC the partial thermal degradation of TEG is observed. For all the TEG samples, the electrical conductivity is more than 6 times higher than EG flakes one. The TEG obtained at 600 ºC demonstrates one of the most ordered structures, the highest expanded volume, low oxidized carbon species, and the highest electrical conductivity value (1670 S cm^{-1}). Therefore, the proposed TEG powder could be used for electrically conductive materials.

Declaration of Competing Interest

The authors declare that they have no known competing financial interests or personal relationships that could have appeared to influence the work reported in this paper.

Acknowledgement

This study was financially supported by the grant CZ.02.1.01/0.0/0.0/16_025/0007414 OPVVV PaC-NG.

Appendix A. Supplementary information.

The following are the Supplementary data to this article:

Supplementary data 1.

References

[1] E.C. Vermisoglou, T. Giannakopoulou, G.E. Romanos, N. Boukos, M. Giannouri, C. Lei, C. Lekakou, C. Trapalis, Non-activated high surface area expanded graphite oxide for supercapacitors, Appl. Surf. Sci. 358 (2015) 110–121. https://doi.org/10.1016/j.apsusc.2015.08.123.

[2] G. Ma, J. Sun, Y. Zhang, Y. Jing, Y. Jia, Preparation and thermal properties of stearic acid-benzamide eutectic mixture/expanded graphite composites as phase change materials for thermal energy storage, Powder Technol. 342 (2019) 131–140. https://doi.org/10.1016/j.powtec.2018.09.074.

[3] S. Tao, S. Wei, Y. Yulan, Characterization of expanded graphite microstructure and fabrication of composite phase-change material for energy storage, J. Mater. Civ. Eng. 27 (2015) 04014156. https://doi.org/10.1061/(ASCE)MT.1943-5533.0001089.

[4] J. Xiang, L.T. Drzal, Thermal conductivity of exfoliated graphite nanoplatelet paper, Carbon N. Y. 49 (2011) 773–778. https://doi.org/10.1016/j.carbon.2010.10.003.

[5] T.H. Wang, T.F. Yang, C.H. Kao, W.M. Yan, M. Ghalambaz, Paraffin core-polymer shell micro-encapsulated phase change materials and expanded graphite particles as an enhanced energy storage medium in heat exchangers, Adv. Powder Technol. 31 (2020) 2421–2429. https://doi.org/10.1016/j.apt.2020.04.006.
[6] G. Hristea, P. Budrugeac, Characterization of exfoliated graphite for heavy oil sorption, J. Therm. Anal. Calorim. 91 (2008) 817–823. https://doi.org/10.1007/s10973-006-7465-x.
[7] N. Gulnura, K. Kenes, O. Yerdos, Preparation of expanded graphite using a thermal method, in: IOP Conf. Ser. Mater. Sci. Eng., 2018: p. 012012. https://doi.org/10.1088/1757-899X/323/1/012012.
[8] A. Bayat, S. Aghamiri, A. Moheb, Oil sorption by synthesized exfoliated graphite (EG), Iran. J. Chem. Eng. 5 (2008) 51–64. http://www.sid.ir/En/VEWSSID/J_pdf/102420080105.pdf.
[9] P. Murugan, R.D. Nagarajan, B.H. Shetty, M. Govindasamy, A.K. Sundramoorthy, Recent trends in the applications of thermally expanded graphite for energy storage and sensors – a review, Nanoscale Adv. 3 (2021) 6294–6309. https://doi.org/10.1039/d1na00109d.
[10] A. Bhattacharya, A. Hazra, S. Chatterjee, P. Sen, S. Laha, I. Basumallick, Expanded graphite as an electrode material for an alcohol fuel cell, J. Power Sources. 136 (2004) 208–210. https://doi.org/10.1016/j.jpowsour.2004.03.003.
[11] B.K. Kakati, A. Ghosh, A. Verma, Efficient composite bipolar plate reinforced with carbon fiber and graphene for proton exchange membrane fuel cell, Int. J. Hydrogen Energy. 38 (2013) 9362–9369. https://doi.org/10.1016/j.ijhydene.2012.11.075.
[12] R.K. Gautam, K.K. Kar, Synergistic effects of carbon fillers of phenolic resin based composite bipolar plates on the performance of PEM fuel cell, Fuel Cells. 16 (2016) 179–192. https://doi.org/10.1002/fuce.201500051.
[13] S.R. Dhakate, R.B. Mathur, S. Sharma, M. Borah, T.L. Dhami, Influence of expanded graphite particle size on the properties of composite bipolar plates for fuel cell application, Energy and Fuels. 23 (2009) 934–941. https://doi.org/https://doi.org/10.1021/ef800744m.
[14] S.R. Dhakate, S. Sharma, R.B. Mathur, A. Info, A low-density graphite-polymer composite as a bipolar plate for proton exchange membrane fuel cells, Carbon Lett. 14 (2013) 40–44. https://doi.org/10.5714/CL.2012.14.1.040.
[15] K. Tsai, H. Kuan, H. Chou, C. Kuan, Preparation of expandable graphite using a hydrothermal method and flame-retardant properties of its halogen-free flame-retardant HDPE composites, J. Polym. Res. 18 (2011) 483–488. https://doi.org/10.1007/s10965-010-9440-2.
[16] J. Huang, Q. Tang, W. Liao, G. Wang, W. Wei, C. Li, Green preparation of expandable graphite and its application in flame-resistance polymer elastomer, Ind. Eng. Chem. Res. 56 (2017) 5253–5261. https://doi.org/10.1021/acs.iecr.6b04860.
[17] A. Yasmin, J. Luo, I.M. Daniel, Processing of expanded graphite reinforced polymer nanocomposites, Compos. Sci. Technol. 66 (2006) 1182–1189. https://doi.org/10.1016/j.compscitech.2005.10.014.
[18] A.S. Mostovoy, A. V Yakovlev, Reinforcement of epoxy composites with graphite- graphene structures, Sci. Rep. 9 (2019) 1–9. https://doi.org/10.1038/s41598-019-52751-z.
[19] L. Du, S.C. Jana, Highly conductive epoxy/graphite composites for bipolar plates in proton exchange membrane fuel cells, J. Power Sources. 172 (2007) 734–741. https://doi.org/10.1016/j.jpowsour.2007.05.088.
[20] G. Tang, X. Liu, Y. Yang, D. Chen, H. Zhang, L. Zhou, P. Zhang, H. Jiang, D. Deng, Phosphorus-containing silane modified steel slag waste to reduce fire hazards of rigid polyurethane foams, Adv. Powder Technol. 31 (2020) 1420–1430. https://doi.org/10.1016/j.apt.2020.01.019.
[21] P. Serp, Carbon, in: Compr. Inorg. Chem. II (Second Ed. From Elem. to Appl., 2013: pp. 323–369. https://doi.org/10.1016/B978-0-08-097774-4.00731-2.
[22] D.D.L. Chung, Review graphite, J. Mater. Sci. 37 (2002) 1475–1489. https://doi.org/https://doi.org/10.1023/A:1014915307738.
[23] Y. Yang, X. Zhang, X. Xu, Preparation and characteristics of expanded graphite, Adv. Mater. Res. 189–193 (2011) 2695–2698. https://doi.org/10.4028/www.scientific.net/AMR.189-193.2695.
[24] G. Chen, W. Weng, D. Wu, C. Wu, J. Lu, P. Wang, X. Chen, Preparation and characterization of graphite nanosheets from ultrasonic powdering technique, Carbon N. Y. 42 (2004) 753–759. https://doi.org/10.1016/j.carbon.2003.12.074.
[25] I.M. Afanasov, O.N. Shornikova, I.I. Vlasov, E. V Kogan, A.N. Seleznev, V. V Avdeev, Porous carbon materials based on exfoliated graphite, Inorg. Mater. 45 (2009) 135–139.

https://doi.org/10.1134/S0020168509020058.
[26] J. Prasad, N.S. Bhattacharyya, K.C.J. Raju, Synthesis and microwave characterization of expanded graphite / novolac phenolic resin composite for microwave absorber applications, Compos. Part B. 42 (2011) 1291–1297. https://doi.org/10.1016/j.compositesb.2011.01.026.
[27] M.G. Roemmler, United States Patent: US 2002/0168314 A1. Method of making expanded graphite with high purity and related products, 2002. https://patents.google.com/patent/US20020168314A1/en.
[28] Y. Zhu, S. Murali, M.D. Stoller, A. Velamakanni, R.D. Piner, R.S. Ruoff, Microwave assisted exfoliation and reduction of graphite oxide for ultracapacitors, Carbon N. Y. 48 (2010) 2118–2122. https://doi.org/10.1016/j.carbon.2010.02.001.
[29] L. Drzal, H. Fukushima, United States Patent: US 8,501,858 B2. Expanded graphite and products produced therefrom, 2013. https://patents.google.com/patent/US8501858B2/en.
[30] N.I. Kovtyukhova, Y. Wang, A. Berkdemir, R. Cruz-Silva, M. Terrones, V.H. Crespi, T.E. Mallouk, Non-oxidative intercalation and exfoliation of graphite by Brønsted acids, Nat. Chem. 6 (2014) 957–963. https://doi.org/10.1038/nchem.2054.
[31] Y.R. Shin, S.M. Jung, I.Y. Jeon, J.B. Baek, The oxidation mechanism of highly ordered pyrolytic graphite in a nitric acid/sulfuric acid mixture, Carbon N. Y. 52 (2013) 493–498. https://doi.org/10.1016/j.carbon.2012.10.001.
[32] A. V Yakovlev, A.I. Finaenov, S.L. Zabud, E. V Yakovleva, Thermally expanded graphite : Synthesis , properties , and prospects for use, Russ. J. Appl. Chem. 79 (2006) 1741–1751. https://doi.org/10.1134/S1070427206110012.
[33] J. Lu, W. Weng, X. Chen, D. Wu, C. Wu, G. Chen, Piezoresistive materials from directed shear-induced assembly of graphite nanosheets in polyethylene, Adv. Funct. Mater. 15 (2005) 1358–1363. https://doi.org/10.1002/adfm.200400298.
[34] B. Hou, H.J. Sun, T.J. Peng, X.Y. Zhang, Y.Z. Ren, Rapid preparation of expanded graphite at low temperature, Xinxing Tan Cailiao/New Carbon Mater. 35 (2020) 262–268. https://doi.org/10.1016/S1872-5805(20)60488-7.
[35] M. Cai, D. Thorpe, D.H. Adamson, H.C. Schniepp, Methods of graphite exfoliation, J. Mater. Chem. 22 (2012) 24992–25002. https://doi.org/10.1039/c2jm34517j.
[36] T.J. Manning, M. Mitchell, J. Stach, T. Vickers, Synthesis of exfoliated graphite from fluorinated graphite using an atmospheric-pressure argon plasma, Carbon N. Y. 37 (1999) 1159–1164. https://doi.org/https://doi.org/10.1016/S0008-6223(98)00316-9.
[37] R. Goudarzi, G. Hashemi Motlagh, The effect of graphite intercalated compound particle size and exfoliation temperature on porosity and macromolecular diffusion in expanded graphite, Heliyon. 5 (2019) e02595. https://doi.org/10.1016/j.heliyon.2019.e02595.
[38] I.M. Afanasov, D. V Savchenko, S.G. Ionov, D.A. Rusakov, A.N. Seleznev, V. V Avdeev, Thermal conductivity and mechanical properties of expanded graphite, Inorg. Mater. 45 (2009) 486–490. https://doi.org/10.1134/S0020168509050057.
[39] T.H. Kim, E.K. Jeon, Y. Ko, B.Y. Jang, B.S. Kim, H.K. Song, Enlarging the d-spacing of graphite and polarizing its surface charge for driving lithium ions fast, J. Mater. Chem. A. 2 (2014) 7600–7605. https://doi.org/10.1039/c3ta15360f.
[40] A.E. Teplykh, S.G. Bogdanov, Y.A. Dorofeev, A.N. Pirogov, Y.N. Skryabin, V.G. Makotchenko, A.S. Nazarov, V.E. Fedorov, Structural state of expanded graphite prepared from intercalation compounds, Crystallogr. Reports. 51 (2006) 62–66. https://doi.org/https://doi.org/10.1134/S1063774506070108.
[41] A.D. Lucking, L. Pan, D.L. Narayanan, C.E.B. Clifford, Effect of expanded graphite lattice in exfoliated graphite nanofibers on hydrogen storage, J. Phys. Chem. B. 109 (2005) 12710–12717. https://doi.org/10.1021/jp0512199.
[42] B. Gurzęda, T. Buchwald, M. Nocuń, A. Bąkowicz, P. Krawczyk, Graphene material preparation through thermal treatment of graphite oxide electrochemically synthesized in aqueous sulfuric acid, RSC Adv. 7 (2017) 19904–19911. https://doi.org/10.1039/c7ra01678f.
[43] G. Zhang, M. Wen, S. Wang, J. Chen, J. Wang, Insights into thermal reduction of the oxidized graphite from the electro-oxidation processing of nuclear graphite matrix, RSC Adv. 8 (2018) 567–579. https://doi.org/10.1039/c7ra11578d.
[44] A. Ganguly, S. Sharma, P. Papakonstantinou, J. Hamilton, Probing the thermal deoxygenation of graphene oxide using high-resolution in situ X-ray-based spectroscopies, J. Phys. Chem. C. 115 (2011) 17009–17019. https://doi.org/10.1021/jp203741y.

[45] S. Tian, J. Sun, S. Yang, P. He, S. Ding, G. Ding, X. Xie, Facile thermal annealing of graphite oxide in air for graphene with a higher C/O ratio, RSC Adv. 5 (2015) 69854–69860. https://doi.org/10.1039/c5ra09388k.
[46] X. Yu, Q. Liwen, Preparation for graphite materials and study on electrochemical degradation of phenol by graphite cathodes, Adv. Mater. Phys. Chem. 2 (2012) 63–68. https://doi.org/10.1166/jnn.2014.8954.
[47] A. Gupta, R.K. Goyal, Electrical properties of polycarbonate/expanded graphite nanocomposites, J. Appl. Polym. Sci. 136 (2019) 1–9. https://doi.org/10.1002/app.47274.
[48] N. Sykam, R.K. Gautam, K.K. Kar, Electrical, mechanical, and thermal properties of exfoliated graphite/phenolic resin composite bipolar plate for polymer electrolyte membrane fuel cell, Polym. Eng. Sci. (2015). https://doi.org/10.1002/pen.23959.
[49] K. Kunz, B. Krause, B. Kretzschmar, L. Juhasz, O. Kobsch, W. Jenschke, M. Ullrich, P. Pötschke, Direction dependent electrical conductivity of polymer/carbon filler composites, Polymers (Basel). 11 (2019). https://doi.org/10.3390/polym11040591.
[50] S.K. Nayak, S. Mohanty, S.K. Nayak, Thermal, electrical and mechanical properties of expanded graphite and micro-SiC filled hybrid epoxy composite for electronic packaging applications, J. Electron. Mater. 49 (2020) 212–225. https://doi.org/10.1007/s11664-019-07681-x.
[51] S.R. Dhakate, S. Sharma, M. Borah, R.B. Mathur, T.L. Dhami, Expanded graphite-based electrically conductive composites as bipolar plate for PEM fuel cell, Int. J. Hydrogen Energy. 33 (2008) 7146–7152. https://doi.org/10.1016/j.ijhydene.2008.09.004.
[52] A. Celzard, J.F. Marêché, G. Furdin, S. Puricelli, Electrical conductivity of anisotropic expanded graphite-based monoliths, J. Phys. D. Appl. Phys. 33 (2000) 3094–3101. https://doi.org/10.1088/0022-3727/33/23/313.
[53] H. Xian, T. Peng, H. Sun, J. Wang, The effect of thermal exfoliation temperature on the structure and supercapacitive performance of graphene nanosheets, Nano-Micro Lett. 7 (2014) 17–26. https://doi.org/10.1007/s40820-014-0014-4.
[54] Gatan Inc., DigitalMicrograph, (1996). https://www.gatan.com.
[55] F. Tuinstra, J. L. Koenig, Characterization of graphite fiber surfaces with Raman spectroscopy, J. Compos. Mater. 4 (1970) 492–497. https://doi.org/https://doi.org/10.1177/002199837000400405.
[56] P. Puech, M. Kandara, G. Paredes, L. Moulin, E. Weiss-Hortala, A. Kundu, N. Ratel-Ramond, J.-M. Plewa, R. Pellenq, M. Monthioux, Analyzing the Raman spectra of graphenic carbon materials from kerogens to nanotubes: What type of information can be extracted from defect bands?, C — J. Carbon Res. 5 (2019) 69. https://doi.org/10.3390/c5040069.
[57] J. Libra, KolXPD, (2003). http://www.kolibrik.net/science/kolxpd.
[58] R. Blume, D. Rosenthal, J.P. Tessonnier, H. Li, A. Knop-Gericke, R. Schlögl, Characterizing graphitic carbon with X-ray photoelectron spectroscopy: A step-by-step approach, ChemCatChem. 7 (2015) 2871–2881. https://doi.org/10.1002/cctc.201500344.
[59] F.M. Smits, Measurement of sheet resistivities with the four-point probe, Bell Syst. Tech. J. 37 (1958) 711–718. https://doi.org/10.1002/j.1538-7305.1958.tb03883.x.
[60] I. Miccoli, F. Edler, H. Pfnür, C. Tegenkamp, The 100th anniversary of the four-point probe technique: The role of probe geometries in isotropic and anisotropic systems, J. Phys. Condens. Matter. 27 (2015). https://doi.org/10.1088/0953-8984/27/22/223201.
[61] Haldor Topsoe, Geometric factors in four point resistivity measurement., 1966.
[62] W. Jiang, G. Nadeau, K. Zaghib, K. Kinoshita, Thermal analysis of the oxidation of natural graphite - effect of particle size, Thermochim. Acta. 351 (2000) 85–93. https://doi.org/10.1016/S0040-6031(00)00416-0.
[63] H.K. Jeong, Y.P. Lee, M.H. Jin, E.S. Kim, J.J. Bae, Y.H. Lee, Thermal stability of graphite oxide, Chem. Phys. Lett. 470 (2009) 255–258. https://doi.org/10.1016/j.cplett.2009.01.050.
[64] M.N. Chernysheva, A.Y. Rychagov, D.Y. Kornilov, S. V. Tkachev, S.P. Gubin, Investigation of sulfuric acid intercalation into thermally expanded graphite in order to optimize the synthesis of electrochemical graphene oxide, J. Electroanal. Chem. 858 (2020) 113774. https://doi.org/10.1016/j.jelechem.2019.113774.
[65] Crystal Software Pty. Ltd., Crystal Studio, (2010). http://www.crystal0studio.com/.
[66] M. Inagaki, Advanced Carbon Materials, in: Handb. Adv. Ceram. Mater. Appl. Process. Prop., Second Edi, Elsevier Inc., 2013: pp. 25–60. https://doi.org/10.1016/B978-0-12-385469-8.00002-2.

[67] C. Suryanarayana, M.G. Norton, Crystal structure determination. II: Hexagonal structures, in: X-Ray Diffr., Springer, Boston, MA, 1998: pp. 125–152. https://doi.org/10.1007/978-1-4899-0148-4_5.
[68] Y. Wang, D.C. Alsmeyer, R.L. McCreery, Raman Ssectroscopy of carbon materials: structural basis of observed spectra, Chem. Mater. 2 (1990) 557–563. https://doi.org/10.1021/cm00011a018.
[69] A.C. Ferrari, Raman spectroscopy of graphene and graphite : Disorder , electron – phonon coupling , doping and nonadiabatic effects, Solid State Commun. 143 (2007) 47–57. https://doi.org/10.1016/j.ssc.2007.03.052.
[70] L.G. Cançado, A. Reina, J. Kong, M.S. Dresselhaus, Geometrical approach for the study of G′ band in the Raman spectrum of monolayer graphene, bilayer graphene, and bulk graphite, Phys. Rev. B - Condens. Matter Mater. Phys. 77 (2008) 1–9. https://doi.org/10.1103/PhysRevB.77.245408.
[71] R.P. Vidano, D.B. Fishbach, L.J. Willis, T.M. Loehr, Observation of Raman band shifting with excitation wavelength for carbons and graphites, Solid State Commun. 39 (1981) 341–344. https://doi.org/https://doi.org/10.1016/0038-1098(81)90686-4.
[72] A.C. Ferrari, and J. Robertson, Interpretation of Raman spectra of disordered and amorphous carbon, Phys. Rev. B. 61 (2000) 14095–14107. https://doi.org/https://doi.org/10.1103/PhysRevB.61.14095.
[73] A.N. Popova, Crystallographic analysis of graphite by X-Ray diffraction, Coke Chem. 60 (2017) 361–365. https://doi.org/10.3103/S1068364X17090058.
[74] M. Dopita, M. Emmel, A. Salomon, M. Rudolph, Z. Matêj, C.G. Aneziris, D. Rafaja, Temperature evolution of microstructure of turbostratic high melting coal-tar synthetic pitch studied using wide-angle X-ray scattering method, Carbon N. Y. 81 (2015) 272–283. https://doi.org/10.1016/j.carbon.2014.09.058.
[75] T. Qiu, J.G. Yang, X.J. Bai, Y.L. Wang, The preparation of synthetic graphite materials with hierarchical pores from lignite by one-step impregnation and their characterization as dye absorbents, RSC Adv. 9 (2019) 12737–12746. https://doi.org/10.1039/c9ra00343f.
[76] M. Dopita, M. Rudolph, A. Salomon, M. Emmel, C.G. Aneziris, D. Rafaja, Simulations of X-ray scattering on two-dimensional, graphitic and turbostratic carbon structures, Adv. Eng. Mater. 15 (2013) 1280–1291. https://doi.org/10.1002/adem.201300157.
[77] K. Jurkiewicz, M. Pawlyta, A. Burian, Structure of carbon materials explored by local transmission electron microscopy and global powder diffraction probes, J. Carbon Res. 4 (2018) 68. https://doi.org/10.3390/c4040068.
[78] O.N. Shornikova, E. V. Kogan, N.E. Sorokina, V. V. Avdeev, The specific surface area and porous structure of graphite materials, Russ. J. Phys. Chem. A. 83 (2009) 1022–1025. https://doi.org/10.1134/S0036024409060260.
[79] C. Liu, Z. Chen, H. Chen, Z. Miao, M. Fu, Preparation of expanded graphite-based composites by one step impregnation, J. Wuhan Univ. Technol. Mater. Sci. Ed. 26 (2011) 253–256. https://doi.org/10.1007/s11595-011-0208-2.
[80] M. Bera, Chandravati, P. Gupta, P.K. Maji, Facile one-pot synthesis of graphene oxide by sonication assisted mechanochemical approach and its surface chemistry, J. Nanosci. Nanotechnol. 18 (2018) 902–912. https://doi.org/10.1166/jnn.2018.14306.
[81] V. Ţucureanu, A. Matei, A.M. Avram, FTIR spectroscopy for carbon family study, Crit. Rev. Anal. Chem. 46 (2016) 502–520. https://doi.org/10.1080/10408347.2016.1157013.
[82] G. Socrates, Infrared and Raman Characterisctic Group Frequencies, Third Edit, Chichester, 2001. https://doi.org/10.1016/0160-9327(81)90159-9.
[83] R.A. Friedel, G.L. Carlson, Infrared spectra of ground graphite, J. Phys. Chem. 75 (1971) 1149–1151. https://doi.org/10.1021/j100678a021.
[84] A. Lazzarini, A. Piovano, R. Pellegrini, G. Leofanti, G. Agostini, S. Rudić, M.R. Chierotti, R. Gobetto, A. Battiato, G. Spoto, A. Zecchina, C. Lamberti, E. Groppo, A comprehensive approach to investigate the structural and surface properties of activated carbons and related Pd-based catalysts, Catal. Sci. Technol. 6 (2016) 4910–4922. https://doi.org/10.1039/c6cy00159a.
[85] A. Lazzarini, R. Pellegrini, A. Piovano, S. Rudić, C. Castan-Guerrero, P. Torelli, M.R. Chierotti, R. Gobetto, C. Lamberti, E. Groppo, The effect of surface chemistry on the performances of Pd-based catalysts supported on activated carbons, Catal. Sci. Technol. 7 (2017) 4162–4172. https://doi.org/10.1039/c7cy01005b.
[86] E. Groppo, F. Bonino, F. Cesano, A. Damin, M. Manzoli, Chapter 4: Raman, IR and INS Characterization of Functionalized Carbon Materials, in: Met. Funct. Carbons Catal. Synth. Charact.

Appl., The Royal Society of Chemistry, 2018: pp. 105–137. https://doi.org/10.1039/9781788013116-00103.
[87] Z. Shengtao, G. Anyan, G. Huanfang, C. Xiangqian, Characterization of exfoliated graphite prepared with the method of secondary intervining, Int. J. Ind. Chem. 2 (2011) 123–130.
[88] Y. Song, Z. Liu, H.K. Mao, R.J. Hemley, D.R. Herschbach, High-pressure vibrational spectroscopy of sulfur dioxide, J. Chem. Phys. 122 (2005) 1–9. https://doi.org/10.1063/1.1883405.
[89] Y.M. Shulga, S.A. Baskakov, E.I. Knerelman, G.I. Davidova, E.R. Badamshina, N.Y. Shulga, E.A. Skryleva, A.L. Agapov, D.N. Voylov, A.P. Sokolov, V.M. Martynenko, Carbon nanomaterial produced by microwave exfoliation of graphite oxide: New insights, RSC Adv. 4 (2014) 587–592. https://doi.org/10.1039/c3ra43612h.
[90] X. Chen, X. Wang, D. Fang, A review on C1s XPS-spectra for some kinds of carbon materials, Fullerenes Nanotub. Carbon Nanostructures. 28 (2020) 1–11. https://doi.org/10.1080/1536383X.2020.1794851.
[91] S. Kaciulis, Spectroscopy of carbon: From diamond to nitride films, Surf. Interface Anal. 44 (2012) 1155–1161. https://doi.org/10.1002/sia.4892.
[92] Y. Hong, Z. Wang, X. Jin, Sulfuric acid intercalated graphite oxide for graphene preparation, Sci. Rep. 3 (2013) 5–10. https://doi.org/10.1038/srep03439.
[93] M. Wahlqvist, A. Shchukarev, XPS spectra and electronic structure of Group IA sulfates, J. Electron Spectros. Relat. Phenomena. 156–158 (2007) 310–314. https://doi.org/10.1016/j.elspec.2006.11.032.
[94] X. Wang, Z. Sun, Y. Zhao, J. Li, Y. Zhang, Z. Zhang, Na4Mn9O18 nanowires wrapped by reduced graphene oxide as efficient sulfur host material for lithium/sulfur batteries, J. Solid State Electrochem. 24 (2020) 111–119. https://doi.org/10.1007/s10008-019-04478-0.
[95] K. Nkrumah-Amoako, E.P.L. Roberts, N.W. Brown, S.M. Holmes, The effects of anodic treatment on the surface chemistry of a Graphite Intercalation Compound, Electrochim. Acta. 135 (2014) 568–577. https://doi.org/10.1016/j.electacta.2014.05.063.
[96] A.M.P. Sakita, R. Della Noce, P.L. Gastelois, W.A.A. Macedo, R. Lassarote Lavall, Binder-free graphitic films with high conductivity for supercapacitor devices, Chem. Eng. J. 427 (2022) 1–21. https://doi.org/10.1016/j.cej.2021.131731.
[97] S. Xu, Z. Zhang, J. Liu, Y. Wang, J. Hu, Facile preparation of reduced graphene by optimizing oxidation condition and further reducing the exfoliated products, J. Mater. Res. 32 (2017) 383–391. https://doi.org/10.1557/jmr.2016.476.